12-2021

Force and torque model sensitivity and coarse graining for bedload-dominated sediment transport

Liheng Guan

Jorge Salinas

Nadim Zgheib

S. Balachandar

Force and torque model sensitivity and coarse graining for bedload-dominated sediment transport

Liheng Guan[a], Jorge Salinas[a,*], Nadim Zgheib[b], S. Balachandar[a]

[a] *Department of Mechanical and Aerospace Engineering, University of Florida, Gainesville, FL 32611, USA*
[b] *School of Engineering, Lebanese American University, Byblos, Lebanon*

Abstract

We present results from Euler-Lagrange simulations of turbulent flow over an erodible monodisperse bed of particles at a shear Reynolds number of $Re_\tau = 180$. The Galileo number Ga and the ratio of Shields to the critical Shields number Θ/θ_{cr} were varied in the range 11.4 to 29.8 and 1.32 to 5.98, respectively. Two drag force models were investigated along with the influence of lift, particle rotation, and tangential collision forces for each model. Both models give similar results as far as mean particle flux and Shields stress are concerned, however we find that excluding particle rotation, without ignoring the associated tangential collisional force, significantly reduces the particle flux with little influence on Shields stress. On the other hand, when both particle rotation and tangential collision forces are not taken into account, the particle flux is practically unchanged, but the excess Shields stress slightly increases compared to the case where both effects are considered. We also find the lift force to substantially influence particle flux. Additionally, we show the importance of spatial coarse graining and time averaging for Euler-Euler simulations and quantify the reduction in scatter for space and time dependent variables such as sediment flux, Shields stress, and bed surface fluid velocities.

Keywords: Sediment transport, Euler-Lagrange simulations, particle-flow simulations, drag model, coarse graining, turbulent flow.

1. Introduction

Sediment particles are set in motion when an erodible particle bed is placed below a turbulent shearing flow. Such flows are ubiquitous in nature and examples include turbidity currents (e.g. [1]), rivers (e.g. [2]), and coastal sea waves (e.g. [3]), to name a few. It is important to estimate the amount of sediment that is transported by such shearing flows (e.g. [4, 5]). Transport can occur as bedload or as suspended load depending on how particles are transported. When transported particles remain at close proximity to the bed and their motion consists primarily of rolling, sliding, and saltation, sediment transport is labeled as bedload (e.g. [6]). Bedload transport occurs when the bed shear stress at the sediment-fluid interface is marginally in excess of the critical shear stress necessary for incipient motion of particles. The bedload transport rate is a statistical quantity and is usually obtained from empirical relations as a function of the non-dimensional shear stress at the bed (e.g. [7, 8]). On the other hand, if the overlying turbulent flow is relatively vigorous such that the bed shear stress is well above the critical shear stress, particles may be entrained into and remain suspended by the flow. This mode of transport is labeled as suspended load (e.g [9]). In the present study, we will restrict our attention to bedload-dominated transport.

Predicting sediment transport at the grain level is a daunting task because of the large variability in the flow velocity around a grain due to turbulent fluctuations in addition to the stochastic arrangement

*Corresponding author
Email address: josalinas@ufl.edu (Jorge Salinas)

of neighboring particles around that grain within the bed (e.g. [10, 11]). However, upon averaging over a large enough area or over long enough times, the variability in both the flow field and the bed arrangement become less important. Under such conditions, simple empirical expressions for the sediment flux can be obtained as a function of the bed shear stress. In fact, many such expressions have been proposed. Meyer-Peter and Müller [5] were among the first to propose an expression for the sediment flux as a function of the excess Shields stress. Their expression came to be known as the "Swiss formula". Wong and Parker [4] (WP) suggested a correction to the Swiss formula, namely $q = 4.93(\theta - \theta_{cr})^{1.6}$, where q is the sediment flux per unit width, θ is the average Shields stress at the sediment bed, and θ_{cr} is the critical Shields stress for incipient motion.

The Swiss formula, and consequently the WP expression, were derived to estimate the sediment flux under temporally- and spatially-averaged conditions. Turbulence-resolved simulations of the flow above a sediment bed is becoming increasingly possible with the application of bedload transport models such as the Swiss formula or the WP expression as the bottom boundary conditions (e.g. [12, 13]). Care however must be taken with such an application. Due to turbulence resolution, the near-bed grid can be of the order of sediment size and correspondingly the time step is small enough for temporal resolution of turbulence. It therefore becomes important to average the turbulent shear stress over space (on the order of a hundred particle diameters) and over time in order to apply the bedload transport models as appropriate boundary conditions [14, 15, 12, 13]. In this study, we start with Euler-Lagrange simulations, where the dynamics of every sediment grain within the computational domain is accurately tracked. The simulations results thus yield highly accurate space and time-dependent bedload transport information that has been obtained with sediment-level resolution. This accurate information is then space-time averaged as a *post-processing* step for different levels of spatial and temporal filter widths. With such a coarse-graining post-processing operation, we plan to compare the average bedload transport obtained from the simulations against the WP expression. We propose to identify an optimal length scale of averaging below which local fluctuations of bedload transport will substantially deviate from that predicted by the model and above which the averaging will match closely the model prediction.

For the sake of clarity, We want to stress that the present simulations do not use the Swiss formula or any other bedload transport correlation. We solve the motion of each and every particle within the bed. The coarse graining operation is only a post-processing step. We also would like to stress the difference between the coarse graining and the filtering process represented by the anisotropic Gaussian filter in (1). The latter is on the order of a few particle diameters, while the former is on the order of 100 particle diameters. The coarse graining filter will not modify the flow nor the sediment transport. The coarse graining operation reveals that only when averaged over lengths of the order of 100 particle diameters the averaged shear stress and the averaged bedload transport are correlated in accordance with the Swiss formula and other such correlations. When averaged over smaller lengths, the departure between average bedload calculated from post-processing the simulations results and that estimated with the Swiss formula increased. Thus the optimal coarse graining filter widths are an order of magnitude larger than the length scale of the feedback filter in (1).

Euler-Lagrange (EL) simulations of particle-laden flows have been used in many physical contexts, from the study of fluidized beds (e.g. [16]) to particle dispersal in sprays (e.g. [17]). Particle-resolved simulations are the best, if they can be afforded, since they resolve all the relevant physics of particle-fluid interaction accurately and only the inter-particle collisional physics is modeled (e.g. [18, 19, 20, 21, 22, 23, 24]). The high computational cost of particle-resolved simulations of particle-laden flows makes EL simulations a useful alternative when modeling flows with large number of particles ($> O(10^6)$). However, adequate selection of closure models for hydrodynamic forces and torques acting on particles is fundamental for accurate modeling of the physics of a specific problem. Dilute flows where volume fraction is small allow for the use of "one way" coupled simulations where particle-particle collisions as well as back-coupling from particles to the surrounding fluid is ignored. On the other hand, flows with high concentration of particles, as in the present work, must use "four-way" coupled simulations that account for the back-coupling from the particles to the fluid and particle-particle collisions. In the present context of bedload transport, the high gradient of volume fraction at the particle bed surface requires models that accurately capture the forces on particles saltating above the surface as well as those rolling and sliding at or below the surface.

Another purpose of this paper is to test the influence of different force models on the accuracy of bedload transport in EL simulations by comparing the resulting mean sediment flux and excess Shields to the Wong and Parker formula [4]. We also test the influence of different force and torque components within the model, specifically the role of such force and torque contributions for accurate representation of sediment flux. These components include the lift force, the tangential collision force, the particle rotation and the associated torque on the particle. Additionally, we examine the effect spatial coarse graining (or spatial averaging) and time averaging on the relation between sediment flux and the excess Shields stress. Existence of a unique relation between the coarse-grained excess Shields stress and sediment flux is important in the implementation of Euler-Euler (EE) simulations where individual sediment grains are not tracked. Furthermore, improved empirical sediment flux correlations such as in [4, 5] can be advanced for use in EE simulations. We quantify the effect of coarse graining and time averaging by computing the standard deviation of the scatter for the sediment flux, the excess Shields stress, and the fluid velocity components at the sediment bed surface.

2. Numerical Model

In the present setup, a large number of monodispersed particles are placed at the bottom of the domain to form a random close-packed bed. The process of generating the bed consists of first placing a layer of hexagonally arranged particles at the bottom of the numerical domain, in which every second particle is lifted by a random vertical distance ranging between one particle radius to one particle diameter. Moreover, these particles, which form the bottommost layer are kept fixed during the simulations to prevent artificial locking of particles in the upper layers. The purpose of such an arrangement is to introduce randomness to the particle distribution inside the bed. The additional layers are generated by conducting a sedimentation simulation in which particles can settle to form the close-packed bed. A schematic representation of the numerical domain is shown in Figure 1. Before the start of the simulation, the bed is frozen, and the flow is allowed to reach a stationary state (see schematic velocity profile $\mathbf{u}_f$ in red). After the flow reaches a stationary state and the particle bed is unfrozen, each simulation is run for sufficiently long time such that accurate statistics can be gathered. When the bed is allowed to evolve, chevron-shaped regions of higher bed elevation initially form at random locations within the bed, due to the action of turbulent vortical structures. Over time these chevron regions link laterally to one another and eventually form spanwise-coherent incipient ripples (e.g.[12, 13, 25]). These ripples grow in height and as they travel downstream adjacent ripples sometimes merge to form a larger ripple (e.g. [26]). But these bedforms appear only after a non-dimensional time of two units, before which the bed remains featureless. During this early period bed-related statistics are obtained by averaging spatially over the horizontal bed as well as over time.

The EL methodology is characterized by a three-dimensional, anisotropic Gaussian filter function $G(\mathbf{x}, \mathbf{x}_p)$, which is used to project the properties of the Lagrangian particles to the Eulerian grid [16],

$$G(\mathbf{x}, \mathbf{x}_p) = \frac{1}{\sigma_x \sigma_y \sigma_z \left(\sqrt{2\pi}\right)^3} \exp\left[-\frac{|x - x_p|^2}{2\sigma_x^2} - \frac{|y - y_p|^2}{2\sigma_y^2} - \frac{|z - z_p|^2}{2\sigma_z^2}\right], \tag{1}$$

where $\mathbf{x} = \{x, y, z\}$ and $\mathbf{x}_p = \{x_p, y_p, z_p\}$. Also, $\sigma_i = \delta_i / \left(2\sqrt{2\ln 2}\right)$, with $i = \{x, y, z\}$ represents the standard deviation of G along the ith direction. Here, δ_i is the kernel width in the ith direction, which is defined as the width of G at half of its maximum value. The filter function G satisfies the following integral constraint

$$\iiint_{\Omega} G(\mathbf{x}, \mathbf{x}_p)\, d\mathbf{x} \to 1 \quad \forall\, \mathbf{x}_p\,, \tag{2}$$

where Ω is a very large ellipsoidal volume centered at $\mathbf{x}_p$. In practical implementation, the volume of integration is limited with a cut-off distance r_c, which is defined as the distance where G decays to a small value ϵ relative to its maximum value. The relation between r_c and δ_i is given by [16]

$$r_c = \frac{\delta_i}{2}\sqrt{-\frac{\ln \epsilon}{\ln 2}}\,. \tag{3}$$

In the simulations, we adjust the Gaussian width δ_i such that it spreads over 5 grid points in any direction. It must be emphasized that the above filter function that is used for the spreading of the Lagrangian sediment-related quantities to the Eulerian grid must be distinguished from the filter function to be later used for coarse graining in the post-processing operation.

The filter function is used to first define the Eulerian particle volume fraction field as follows

$$\phi(\mathbf{x}, t) = \sum_{n=1}^{N_p} G\left(\mathbf{x}, \mathbf{x}_{p,n}\right) V_p \,, \tag{4}$$

where $\mathbf{x}_{p,n}$ is the location of the nth particle, $V_p = \frac{\pi}{6} d_p^3$ is the particle volume, and d_p is the particle diameter. Though the summation is formally defined over all the N_p particles within the computational domain, it is only carried out over the n_p particles that are in the neighborhood of point $\mathbf{x}$, whose Gaussian has a non-zero influence. Thus, the filter function allows the definition of a smooth volume fraction field from the discrete Lagrangian particles and this process will be applied to other Lagrangian quantities as well, when needed. A schematic profile of the mean particle volume fraction $\langle\phi\rangle$ (in green) is also shown in Figure 1, where the angle brackets indicate an ensemble average over the horizontal directions and over time. In the following sections, the dimensionless governing equations for the particle and fluid phases are presented. Here and throughout the manuscript, the asterisk denotes dimensional quantities, and all other quantities are to be understood as non-dimensional. The length scale H_f^* is taken as the mean flow depth, and the velocity scale U_τ^* as the mean shear velocity at the particle bed surface, which is defined as the vertical location where the particle volume fraction attains a value of $\phi = 0.1$ (e.g. [20]).

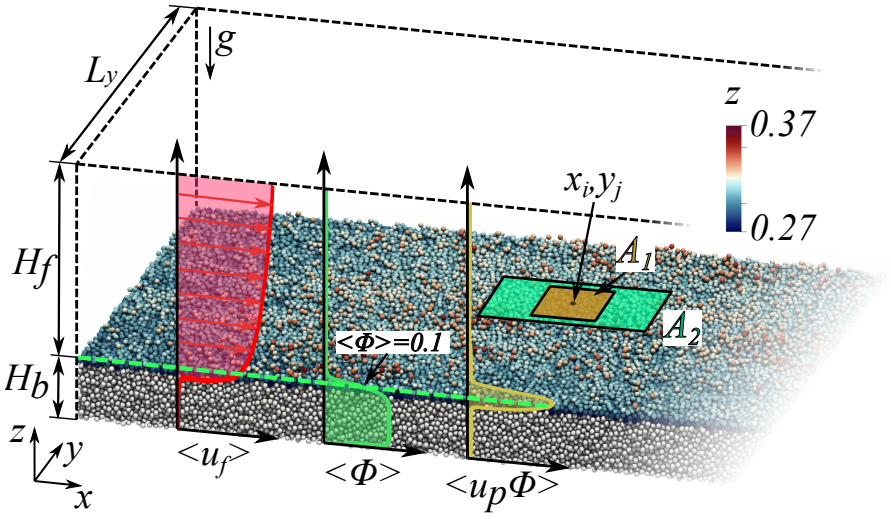

Figure 1: Isometric view of a portion of the numerical domain. The uppermost layer of the particle bed is colored by the particle's vertical location. Schematics of mean profiles of the streamwise component of the flow, volume fraction, and particle flux are shown in red, green, and yellow, respectively. A_1 and A_2 highlight two surfaces centered at (x_i, y_j) with different areas and aspect ratios overwhich coarse graining is implemented.

2.1. Particle Motion

The motion of the Lagrangian particles is computed by evaluating the forces and torques acting on them and integrating the following equations for the particle positions $\mathbf{x}_p = \mathbf{x}_p^*/H_f^*$, center velocities $\mathbf{v}_p = \mathbf{v}_p^*/U_\tau^*$,

and angular velocities $\boldsymbol{\omega}_p = \boldsymbol{\omega}_p^*/(U_\tau^*/H_f^*)$,

$$\frac{d\mathbf{x}_p}{dt} = \mathbf{v}_p, \tag{5}$$

$$\frac{\pi}{6}\beta d_p^3 \frac{d\mathbf{v}_p}{dt} = \mathbf{F}_{un} + \mathbf{F}_d + \mathbf{F}_l + \mathbf{F}_{am} + \mathbf{F}_c + \mathbf{F}_b, \tag{6}$$

$$I_p \frac{d\boldsymbol{\omega}_p}{dt} = \mathbf{T}_h + \mathbf{T}_c + \mathbf{T}_r. \tag{7}$$

In the above, $\beta = \rho_p^*/\rho_f^*$ is the ratio of particle (ρ_p^*) to fluid (ρ_f^*) density. In this work, particles are taken to be spheres of diameter $d_p = d_p^*/H_f^*$. As a result, the particle moment of inertia is $I_p = \frac{\pi}{60}\beta d_p^5$.

In equation 6, the terms on the right-hand side correspond to the undisturbed force ($\mathbf{F}_{un}$), the drag force ($\mathbf{F}_d$), the lift force ($\mathbf{F}_l$), the added-mass force ($\mathbf{F}_{am}$), the particle-particle and particle-wall collision force ($\mathbf{F}_c$), and the body force ($\mathbf{F}_b$). As for equation 7, $\mathbf{T}_h$, $\mathbf{T}_c$, and $\mathbf{T}_r$ represent the hydrodynamic, collision, and rolling torques, respectively.

2.1.1. Undisturbed Flow Force

The undisturbed flow force, $\mathbf{F}_{un}$, depends on the ambient flow conditions.

$$\mathbf{F}_{un} = -V_p \nabla p, \tag{8}$$

where ∇p is the fluid pressure gradient as computed in the EL simulation interpolated to the particle center. Note that the fluid pressure p is obtained after subtracting the hydrostatic component and thus the buoyancy force is explicitly included in the definition of the body force. When evaluating this and other hydrodynamic force contributions, fluid quantities such as ∇p (and later fluid velocity and fluid acceleration) are required at the particle locations. These fluid properties are interpolated from the Eulerian grid to the center of the particle using trilinear interpolation, which uses the eight Eulerian grid points surrounding the particle center in question.

2.1.2. Quasi-steady Drag Force

The quasi-steady drag force $\mathbf{F}_d$ is perhaps the most dominant of all the hydrodynamic force contributions and it arises from the flow disturbance due to the presence of the particle. The drag force is a function of the velocity difference between the ambient flow and the particle but it is also influenced by the presence of neighboring particles. The drag correlation of an isolated particle as a function of particle Reynolds number, which can be considered as a non-dimensional measure of relative velocity, has been well established (e.g. [27]). Although correlations of mean drag have been advanced taking into account the effect of neighboring particles (e.g. [28]), there still remains considerable differences between the different correlations. Furthermore, these correlations are intended for homogeneous systems where particle volume fraction remains spatially uniform. The problem of bedload transport presents a different scenario where there is strong volume fraction variation at the surface of the bed, where the particle motion is strong. We consider two different models of drag force that will be tested in the present work.

First, we test a simple model originally designed to compute drag on particles where the volume fraction is homogeneous in the domain [29]

$$\mathbf{F}_{d1} = \frac{3\pi d_p \left(\mathbf{u}_f - \mathbf{v}_p\right)}{Re_\tau} \Phi\left(\phi, Re_p\right), \tag{9}$$

where $\mathbf{u}_f$ is the fluid velocity at the particle center and $Re_\tau = U_\tau^* H_f^*/\nu^*$ is the shear Reynolds number. ν^* here represents the fluid kinematic visocity, and $\Phi\left(\phi, Re_p\right)$ is the correction factor to the steady Stokes drag to account for the finite Reynolds number and finite volume fraction. In the present work, Φ is modeled as a function of the particle volume fraction ϕ and the particle Reynolds number Re_p [29]

$$\Phi\left(\phi, Re_p\right) = \begin{cases} \frac{1-2\phi}{(1-\phi)^3}\left(1 + 0.15Re_p^{0.687} + \frac{0.42}{1+42500/Re_p^{1.16}}\right), & \text{if } \phi \leq 0.2 \\ 1.172\left(1 + 0.15Re_p^{0.687} + \frac{0.42}{1+42500/Re_p^{1.16}}\right), & \text{if } \phi > 0.2 \end{cases} \tag{10}$$

where the particle Reynolds number Re_p is given by

$$Re_p = Re_\tau \, |\mathbf{u}_f - \mathbf{v}_p| \, d_p. \tag{11}$$

Instead of the above expression, where the volume fraction correction was based on the analytical results of [30], we could instead use one of the more recent correlations by [28, 31].

The second model for drag force tested in this work, and the one used in most of our simulations is of a different flavor. This model's primary focus are the mobile particles that roll on the surface of the bed or those that are in saltation motion. We use the model proposed by [32] and [33] that is designed to compute drag on a particle at a distance δ over a bed of particles (see schematics in Figure 2a)

$$\mathbf{F}_{d2} = \frac{\pi}{8} C_D d_p^2 \, |\mathbf{u}_f - \mathbf{v}_p| \, (\mathbf{u}_f - \mathbf{v}_p) \, , \tag{12}$$

where the subscript '2' in the force indicates the second model. The drag coefficient C_D is computed as

$$C_D = \frac{24}{Re_p} \left[1 + 0.138 \exp(-2\delta/d_p) + \frac{9}{16(1 + 2\delta/d_p)} \right] \left(1 + \alpha_D Re_p^{\beta_D} \right) , \tag{13}$$

where

$$\alpha_D = 0.15 - 0.046 \left(1 - 0.16(\delta/d_p)^2 \right) \exp\left(-0.7\delta/d_p \right) \tag{14}$$

$$\beta_D = 0.687 + 0.066 \left(1 - 0.76)(\delta/d_p)^2 \right) \exp\left(-(\delta/d_p)^{0.9} \right) \tag{15}$$

The above correlation was originally developed for a laminar shear flow past a spherical particle sitting over a flat wall [34], in which case δ was defined as the gap between the bottom of the particle and the flat wall. The applicability of the above correlation in a turbulent flow was then established through particle-resolved simulations of wall turbulence over a spherical particle sitting on a flat wall [33]. The problem of a particle sitting on a rough wall made up of similar-sized particles was then considered by [35] in the laminar flow regime and by [32] in the turbulent flow regime. These particle-resolved investigations confirmed that the above drag correlation provided adequate description of the instantaneous force on the particle, provided δ is defined as the distance between the bottom of the particle and the *bed level*. The bed level is defined as the lowest point to which the bottom of the particle could be lowered to, which for a sheet of monodispersed particles correspond to a height of $0.3165 d_p$ from the plane of the centers of the bed-particles.

For a hexagonally packed layer of particles the bed level corresponds to a volume fraction of about $\phi = 0.4$. The value of ϕ corresponding to the bed level decreases for a random arrangement of particles. We simply take δ to be the normal distance from the surface of $\phi = 0.1$ to the bottom of the particle, whose quasi-steady force is being evaluated. Particles whose δ is negative are taken to be inside the bed. When a particle is deep inside the bed, then its neighborhood can be considered locally homogeneous at the local volume fraction. Nevertheless, the flow inside the bed is far weaker and therefore we take the hydrodynamic force on the particles to be evaluated with δ/d_p set to zero, making C_D solely a function of particle Reynolds number Re_p.

2.1.3. Quasi-steady Lift Force

The lift force on a particle can arise from three sources: (i) shear-induced lift due to ambient shear or vorticity, (ii) wall-induced lift due to the motion of a particle near a wall, or in this case a bed of stationary particles, and (iii) rotation-induced Magnus lift force due to the rotation of the particle [36, 10]. For a particle in incipient motion, the shear-induced lift is the dominant contribution. However, it has been established that the intensity of the shear-induced lift force is substantially modified by the presence of a nearby boundary. We follow the approach pursued in the second drag model and define the shear-induced lift force as [37]

$$\mathbf{F}_l = \frac{\pi}{8} C_L d_p^2 (\delta + \frac{d_p}{2}) \left[(\mathbf{u}_f - \mathbf{v}_p) \times \mathbf{\Omega} \right] , \tag{16}$$

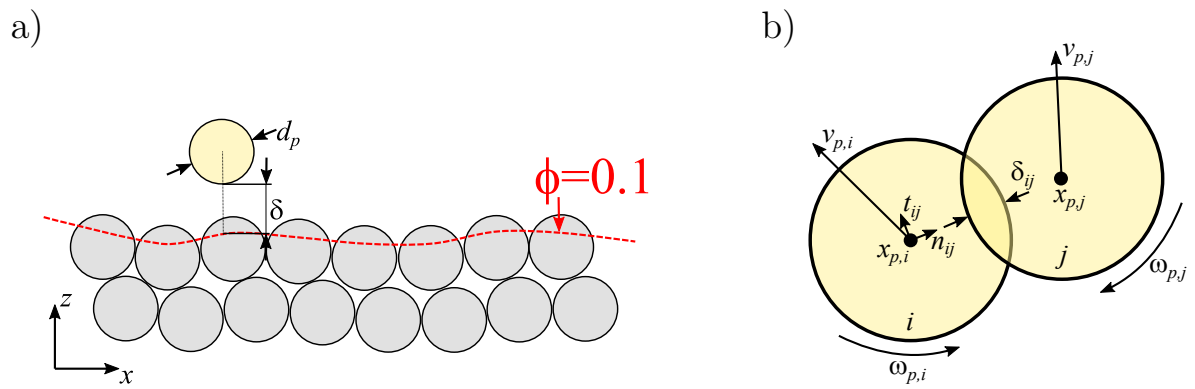

Figure 2: a) Schematics of particle moving of bed of particles; b) Schematic diagram of collision between a pair of particles.

where $\mathbf{\Omega} = \nabla \times \mathbf{u}_f$ is the vorticity at the particle's center. The lift coefficient is computed as [32]

$$C_L = \frac{3.663}{(Re_p^2 + 0.1173)^{0.22}} \exp\left[-0.5(\delta/d_p)\left(\frac{Re_p}{250}\right)^{4/3}\right]\left[\exp(\alpha_L(\delta/d_p)^{\beta_L}) - \lambda_L\right], \tag{17}$$

where

$$\alpha_L = -\exp\left(-0.3 + 0.025Re_p\right), \tag{18}$$

$$\beta_L = 0.8 + 0.01Re_p, \tag{19}$$

$$\lambda_L = \left[1 - \exp(-\delta/d_p)\right]\left(\frac{Re_p}{250}\right)^{5/2}. \tag{20}$$

The lift force was also originally obtained from particle-resolved simulations of a laminar linear shear flow past a spherical particle sitting on a flat wall [34]. This correlation was later extended to be applicable for a particle sitting on a rough wall in a turbulent flow [33, 35, 32].

2.1.4. Added-Mass and Body Forces

As for the added-mass force $\mathbf{F}_{am}$, it arises from the relative acceleration between the ambient flow and the particle. The model for this force is [38]

$$\mathbf{F}_{am} = C_m V_p \left(\frac{D\mathbf{u}_f}{Dt} - \frac{d\mathbf{v}_p}{dt}\right), \tag{21}$$

where $D\mathbf{u}_f/Dt$ is the material or total derivative of the fluid macroscale velocity computed in the EL approach evaluated at the particle's center and the added-mass coefficient $C_m = 1/2$. This expression for added-mass force is strictly applicable for an isolated particle. Clearly, the presence of neighboring particles will alter the value of the added-mass coefficient to be different from 1/2. Here we ignore this influence, since we do not have adequate knowledge of the added-mass effect on a particle sitting on a flat or a rough wall. We also ignore the history effect. Fortunately, the acceleration of the flow and the particle are sufficiently mild in the present application that both the added-mass and history forces are quite small compared to the quasi-steady force.

Finally, $\mathbf{F}_b$ is the body force of the particle. In the present work, $\mathbf{F}_b$ can be computed as the difference between the gravitational force and the buoyancy force, which in its dimensionless form reduces to

$$\mathbf{F}_b = \frac{\pi}{6} d_p^2 \frac{1}{\Theta} \mathbf{e}_g, \tag{22}$$

where $\mathbf{e}_g$ is a unit vector in the direction of gravity and Θ is the Shields number imposed by the flow,

$$\Theta = \frac{U_\tau^{*2}}{Rg^* d_p^*}. \tag{23}$$

Here, g^* is the magnitude of the gravitational acceleration and $R = \rho_p^*/\rho_f^* - 1$ is the submerged specific gravity of the particles. Note that Θ is an input to the simulations and accounts for the ratio between the shear and gravitational forces. As Θ increases, the particle body force decreases and the flow is able to move particles more easily.

2.1.5. Collisional Force

In the present setup, the large number of monodispersed particles form a random near-close-packed bed and as a result, particle-particle collisions occur very frequently within the bed. In order to account for the collision forces in a physically realistic way, a soft-sphere spring-damper model is implemented. This type of model has been extensively used (e.g. [39], [18], [38]). To describe the model, we consider two colliding particles labeled i and j in the schematic of Figure 2b. The particle centers are located at $\mathbf{x}_{p,i}$ and $\mathbf{x}_{p,j}$. At the time instance shown, the particles are rotating with angular velocities $\boldsymbol{\omega}_{p,i}$ and $\boldsymbol{\omega}_{p,j}$, and the particle center velocities are $\mathbf{v}_{p,i}$ and $\mathbf{v}_{p,j}$. The collision model allows for particles to have a slight overlap, which is defined as

$$\delta_{ij} = 0.5\left(d_{p,i} + d_{p,j}\right) - \left|\mathbf{x}_{p,i} - \mathbf{x}_{p,j}\right|, \tag{24}$$

where $\mathbf{n}_{ij}$ is the unit normal vector which points from particle i to particle j, through the centers of the two particles

$$\mathbf{n}_{ij} = \frac{\mathbf{x}_{p,j} - \mathbf{x}_{p,i}}{\left|\mathbf{x}_{p,j} - \mathbf{x}_{p,i}\right|}. \tag{25}$$

The relative velocity between the two particles at the point of contact can be computed as

$$\mathbf{v}_{p,ij} = \mathbf{v}_{p,i} - \mathbf{v}_{p,j} + \left(0.5 d_{p,i}\boldsymbol{\omega}_{p,i} + 0.5 d_{p,j}\boldsymbol{\omega}_{p,j}\right) \times \mathbf{n}_{ij}. \tag{26}$$

This relative velocity can be decomposed into a normal component $\mathbf{v}_{p,ij}^n$ and a tangential component $\mathbf{v}_{p,ij}^t$. These components are given by

$$\mathbf{v}_{p,ij}^n = \left(\mathbf{v}_{p,ij} \cdot \mathbf{n}_{ij}\right)\mathbf{n}_{ij} \quad \text{and} \quad \mathbf{v}_{p,ij}^t = \mathbf{v}_{p,ij} - \mathbf{v}_{p,ij}^n. \tag{27}$$

We define the tangential unit vector $\mathbf{t}_{ij}$ to point in the direction of $\mathbf{v}_{p,ij}^t$ as

$$\mathbf{t}_{ij} = \frac{\mathbf{v}_{p,ij}^t}{\left|\mathbf{v}_{p,ij}^t\right|}. \tag{28}$$

The total collision force, $\mathbf{F}_c$, acting on particle i represents the summation of normal and tangential collision forces resulting from collisions with neighboring particles.

$$\mathbf{F}_c = \sum_{j \neq i} \mathbf{F}_{c,ij}^n + \mathbf{F}_{c,ij}^t, \tag{29}$$

where $\mathbf{F}_{c,ij}^n$ and $\mathbf{F}_{c,ij}^t$ are the normal and tangential components of the collision force between particles i and j, respectively. The normal collision force $\mathbf{F}_{c,ij}^n$ can be modeled as a linear spring-damper system,

$$\mathbf{F}_{c,ij}^n = \begin{cases} -k_c \delta_{ij}\mathbf{n}_{ij} - \eta_n \mathbf{v}_{p,ij}^n & \text{if } \delta_{ij} > 0, \\ 0 & \text{otherwise.} \end{cases} \tag{30}$$

The first term on the right-hand side is the elastic part of the normal force component and its magnitude is proportional to the overlap distance δ_{ij}. The dimensionless spring stiffness coefficient k_c is defined as

$$k_c = \frac{k_c^*}{\rho_f^* H_f^* U_\tau^{*2}}. \tag{31}$$

In terms of spring stiffness coefficient, a simple estimate of non-dimensional collisional time during which the colliding particles are in contact can be obtained as $t_c = 2(\pi d_p)^{3/2}/\sqrt{6k_c}$. To ensure adequate resolution of particle collisions, k_c has been chosen such that $t_c \approx 10\Delta t$, where Δt is the simulation time step. In the force expression, the second term on the right-hand side is the dissipative part of the normal force component. It is a linear function of the normal component of relative particle velocity. The parameter η_n is the damping coefficient in the normal direction. According to [38], it can be computed based on the spring stiffness coefficient k_c, the normal coefficient of restitution e_n, and the mass of particles involved in the collision,

$$\eta_n = \frac{-2\ln e_n}{\sqrt{\pi^2 + (\ln e_n)^2}} \sqrt{k_c \frac{\pi}{6} \beta \frac{d_{p,i}^3 d_{p,j}^3}{d_{p,i}^3 + d_{p,j}^3}}. \tag{32}$$

The values of k_c and e_n used in the present work are 507 and 0.3, respectively [18].

The Bagnold number Ba plays an important role in asessing the importance of collisional stresses. The Bagnold number is computed as [40]

$$Ba = \beta Re_\tau \lambda^{\frac{1}{2}} d_p^2 \frac{du_p}{dz}, \tag{33}$$

where λ is expressed as

$$\lambda = \frac{1}{(C_0/C)^{1/3} - 1}. \tag{34}$$

Here, C is the average ratio of the sediment-occupied space to the whole space within the bed and C_0 is the maximum possible static volume concentration, which for spheres reach a value of about 0.64. The maximum value of the Bagnold number for the different cases ranges from around 30 to about 200. These estimates will somewhat decrease if we consider the value of C to decrease at the very top of the bed, while the estimates will somewhat increase in regions of more intense turbulence where the local shear is large. Nevertheless, according to [40], our simulations fall in the macro-viscous to transitional regime. In these regimes, the coefficient of restitution has been found to range between 0 and 0.65 [41]. We also emphasize that the conditions of the present simulations are similar to those of particle-resolved simulations of [20], whose collision model along with the value of coefficient of restitution have been adopted here. We should also note that the simulation results continue to reinforce the notion that when grains are flowing the details of the granular rheology are not critical to predicting the bulk statistics of the flow, but rather the bulk energy dissipation is the key factor. This is accounted for in the present simulations by using a value of 0.3 for the coefficient of restitution, which appears to be a suitable average value as the actual coefficient of restitution for individual collisions would range from 0 to 0.65.

The tangential component of the collision force is computed as indicated by [18]

$$\mathbf{F}_{c,ij}^t = \begin{cases} -\left[min\left(\mu_c \left|\mathbf{F}_{c,ij}^n\right|, \eta_t \left|\mathbf{v}_{p,ij}^t\right|\right)\right] \mathbf{t}_{ij} & \text{if } \left|\mathbf{v}_{p,ij}^t\right| \neq 0, \\ 0 & \text{otherwise,} \end{cases} \tag{35}$$

where $\mu_c = 0.4$ [18] is the friction coefficient and η_t is the damping coefficient in the tangential direction. In the present work, η_t is chosen to be the same as η_n [18]. It has been shown in the literature that these values of collisional parameters are appropriate for sediment migration in water and that the results are not sensitive to their variation [18].

2.1.6. Torques

Now, we shift our attention to the evaluation of torques for application in the particle angular momentum equation, equation 7. First, the hydrodynamic torque $\mathbf{T}_h$ can be computed as in [38],

$$\mathbf{T}_h = I_p \frac{60}{64\pi} \frac{1}{\beta} C_t \left|\boldsymbol{\omega}_{rel}\right| \boldsymbol{\omega}_{rel}, \tag{36}$$

where $\boldsymbol{\omega}_{rel}$ is the relative rate of rotation in a viscous fluid,

$$\boldsymbol{\omega}_{rel} = \frac{1}{2}\boldsymbol{\Omega} - \boldsymbol{\omega}_p. \tag{37}$$

The hydrodynamic torque coefficient C_t can be computed as

$$C_t = \frac{C_{t1}}{\sqrt{Re_r}} + \frac{C_{t2}}{Re_r} + C_{t3} Re_r, \tag{38}$$

where the coefficients C_{t1}, C_{t2} and C_{t3} are chosen from Table 1. These coefficients are a function of particle

Re_r	C_{t1}	C_{t2}	C_{t3}
$Re_r < 1$	0	16π	0
$1 \leq Re_r < 10$	0	16π	0.0418
$10 \leq Re_r < 20$	5.32	37.2	0
$20 \leq Re_r < 50$	6.44	32.2	0
$50 \leq Re_r < 100$	6.45	32.1	0

Table 1: Values of the hydrodynamic torque coefficients [38].

rotational Reynolds number Re_r, defined as

$$Re_r = \frac{d_p^2 \left|\boldsymbol{\omega}_{rel}\right| Re_\tau}{4}. \tag{39}$$

The tangential collision force described in the previous section will induce a collision torque on particle i [38],

$$\mathbf{T}_c = \sum_{j \neq i} \frac{d_{p,i}}{2} \mathbf{n}_{ij} \times \mathbf{F}^t_{c,ij}. \tag{40}$$

The rolling torque T_r is also included in equation 7 to account for the rolling resistance on particle i [38]

$$\mathbf{T}_r = \sum_{j \neq i} -\vartheta_r \left|\mathbf{F}^n_{c,ij}\right| r_{ij} \frac{\boldsymbol{\omega}_\Delta}{|\boldsymbol{\omega}_\Delta|}. \tag{41}$$

This torque is in the direction of relative angular velocity $\boldsymbol{\omega}_\Delta = \boldsymbol{\omega}_{p,i} - \boldsymbol{\omega}_{p,j}$. Here $\vartheta_r = 0.06$ [38] is the coefficient of rolling friction, and $r_{ij} = \frac{d_{p,i} d_{p,j}}{2(d_{p,i}+d_{p,j})}$ is the reduced radius. For the case of particle-wall collision, the reduced radius and relative angular velocity become $r_{ij} = d_{p,i}/2$ and $\boldsymbol{\omega}_\Delta = \boldsymbol{\omega}_{p,i}$, respectively.

2.2. Fluid Motion

In the EL approach, the flow on the scale of the particles is not resolved and thus the fluid phase governing equations have been averaged by a filtering operation [42, 43]. Here the filter function has been chosen to be the Gaussian filter defined earlier in equation 1. Unlike the particle-resolved velocity and pressure fields which are only defined in the region occupied by the fluid, the filtered velocity and pressure fields $\mathbf{u}_f$ and p are defined over the entire volume, including the regions inside the particle and thus the filtered governing equations are solved over the entire cuboidal computational domain. The Gaussian filtered dimensionless conservation equations of mass and momentum of the fluid phase are

$$\nabla \cdot \mathbf{u}_f = -\frac{1}{\phi_f} \frac{D\phi_f}{Dt} \tag{42}$$

$$\frac{D\mathbf{u}_f}{Dt} = \mathbf{G} - \nabla p + \frac{1}{Re_\tau} \nabla^2 \mathbf{u}_f + \frac{\mathbf{f}_{pf}}{\phi_f}. \tag{43}$$

Here $p = p^*/\rho_f^* U_\tau^{*2}$ is the perturbation pressure after subtraction of the hydrostatic contribution. $\phi_f = 1 - \phi$ and $\mathbf{u}_f$ are the volume fraction and velocity of the fluid phase, respectively. The anisotropic filtering operation and the interaction of the filter with the top and bottom computational boundaries lead to additional commutation terms in the governing equations, which are commonly ignored. Here we also ignore the Reynolds stress term arising from the sub-grid velocity fluctuations. Following this standard procedure

we obtain the above standard approximate form of the filtered EL equations. In all our simulations we impose a constant non-dimensional streamwise external pressure gradient $\mathbf{G} = (1, 0, 0)$ which drives the flow. The shear Reynolds number $Re_\tau = 180$ is the same for all simulations [44]. The back-coupling of hydrodynamic force from the particle to the fluid $\mathbf{f}_{pf} = \mathbf{f}^*_{pf}/(\rho^*_f U^{*2}_\tau / H^*_f)$ is defined as

$$\mathbf{f}_{pf} = -\sum_{n=1}^{n_p} G\left(\mathbf{x}, \mathbf{x}_p\right)\left(\mathbf{F}_d + \mathbf{F}_l + \mathbf{F}_{am}\right), \tag{44}$$

where n_p is the number of particles that influence the position $\mathbf{x}$ in the Eulerian reference frame. Note that only the perturbation hydrodynamic force contributions from quasi-steady drag, lift and added-mass forces must be applied back onto the fluid.

2.3. Problem Setup

The fluid and particle equations are solved using a highly scalable spectral element solver [45, 46, 16] with a domain size $L_x \times L_y \times L_z = 4\pi \times 4\pi/3 \times 1.31$ along the streamwise, spanwise, and vertical directions. The domain is discretized using $30 \times 30 \times 13$ hexahedral elements with 12^3 Gauss-Lobatto-Legendre (GLL) grid points within each element. This gives a total of ≈ 20.2 million grid points per simulation. Unless otherwise stated, data that is spatially averaged over the entire horizontal plane and temporally averaged from $t = 0.5$ to $t = 2$ is presented with angular brackets $\langle\cdot\rangle$. The chosen time duration over which quantities are averaged is long enough to account for turbulent fluctuations but short enough so that the particle bed remains featureless. Furthermore, a vector quantity with an x or y subscript denotes respectively the streamwise and spanwise components of that vector quantity. Such vector quantities include the Shields number $\boldsymbol{\theta} = \boldsymbol{\tau}^*/(R\, g^* d^*_p)$, defined in terms of the bed shear stress $\boldsymbol{\tau}^*$, and the sediment flux per unit width

$$\mathbf{q}\left(x, y, t\right) = \int_0^{L_z} \left(\sum_{n=1}^{n_p} G\left(\mathbf{x}, \mathbf{x}_p\right) \mathbf{v}_p V_p \right) dz, \tag{45}$$

where the integrand is the Eulerian-phase weighted particle velocity field $\mathbf{u}_p\phi$. The projected particle velocity field $\mathbf{u}_p = \{u_p, v_p, w_p\}$.

Periodic boundary conditions are applied for both the fluid and particle phases along the horizontal directions. For the fluid phase this implies that the velocity and perturbation pressure fields on the left (or front) face of the computational domain is the same as the right (or back) face. For the Lagrangian particles this implies that a particle whose center exits the right (or back) face will be reintroduced into the computational domain from the left (or front) face. The periodic nature of the problem is also recognized in the application of the filter function and as a result Eulerian quantities derived from the Lagrangian particles, such as $\phi(\mathbf{x}, t)$ are also periodic. The periodic nature of the problem is also observed in detecting collisions across the lateral boundaries of the computational domain [47, 16].

3. Results and discussion

The simulations consist of a particle bed composed of nearly 1.3 million particles of dimensionless diameter $d_p = 0.025$ below a unidirectional open-channel turbulent flow. Ten simulations are considered, the details of which are shown in Tables 2, 3, and 4. The Galileo number is defined as $Ga = \sqrt{R g^* d^{*3}_p}/\nu^*$. In the present study, the particle and fluid densities are chosen to be $\rho^*_p = 1.57\, g/cm^3$ and $\rho^*_f = 1.00\, g/cm^3$, and consequently, $R = 0.57$ is fixed for all simulations. Furthermore, we use $g^* = 9.81\, m/s^2$ and $\nu^* = 10^{-6}\, m^2/s$ for all simulations. The value of d^*_p varies from one simulation to the other, however the non-dimensional particle diameter remains fixed as stated earlier. The critical Shields number can be computed as $\theta_{cr} = \frac{1}{2}[0.22 Ga^{-0.6} + 0.06 \exp(-17.77 Ga^{-0.6})]$ [8]. We should note here that each simulation corresponds to a unique set of physical parameters [12, 13], which are shown in Table 3.

We should note here that we use spectral element methodology. Furthermore, based on the smallest element, the grid resolution along different directions are $\Delta x = 0.038$, $\Delta y = 0.013$ and $\Delta z = 0.0027$. Since

the particle diameter is 0.025, this yields $d_p/\Delta x = 0.66$, $d_p/\Delta y = 1.97$, and $d_p/\Delta z = 9.31$. However, it should be also pointed out that the feedback force has been smoothened with an anisotropic filter whose size is $9d_p$, $3d_p$, and $1.2d_p$ along the streamwise, spanwise, and vertical directions. The size of the filter is on the same order as that used in similar studies [39, 48]. Thus, due to the finite size of the particles, an approximation is made in calculating particle forces, since the local fluid velocity is somewhat influenced by the self-induced flow of each particle. Recent works [43] have devised ways to reduce this self-induced effect. The correction is however of the order of other uncertainties that are involved in the force modeling, and is not taken into account in the present work.

Case	d_p	R	Ga	θ_{cr}	Θ	Θ/θ_{cr}	Re_τ	$L_x \times L_y \times L_z$	$N_x \times N_y \times N_z$
$EL1$	0.025	0.57	29.8	0.0173	0.0229	1.32	180	$4\pi \times 4\pi/3 \times 1.31$	$360 \times 360 \times 156$
$EL2$	0.025	0.57	21.0	0.0194	0.0457	2.36	180	$4\pi \times 4\pi/3 \times 1.31$	$360 \times 360 \times 156$
$EL3$	0.025	0.57	14.9	0.0227	0.0914	4.04	180	$4\pi \times 4\pi/3 \times 1.31$	$360 \times 360 \times 156$
$EL4$	0.025	0.57	11.4	0.0260	0.1554	5.98	180	$4\pi \times 4\pi/3 \times 1.31$	$360 \times 360 \times 156$

Table 2: Details of the numerical simulation. Please see text for definitions. L_x, L_y, L_z and N_x, N_y, N_z correspond to the domain size and number of grid points along the streamwise, spanwise, and vertical directions, respectively.

Case	d_p^* (μm)	ρ_p^* (g/cm^3)	ρ_f^* (g/cm^3)	U_τ^* (cm/s)	H_f^* (cm)	H_b^* (cm)	N_p $(million)$
$EL1$	541	1.57	1.00	0.83	2.16	0.670	1.30
$EL2$	429	1.57	1.00	1.05	1.72	0.559	1.30
$EL3$	341	1.57	1.00	1.32	1.36	0.442	1.30
$EL4$	286	1.57	1.00	1.58	1.14	0.353	1.30

Table 3: Physical parameters corresponding to the non-dimensional parameters in Table 2. The choice of the sediment density is motivated by previous studies [49, 50].

3.1. Sensitivity analysis

We present in Table 4 seven different simulations of case EL3 where we test different models for the closure of particle equations of motion. The second column shows the particle motion equations that are solved for each case, while the third column shows the force and torque models that are implemented.

In case EL3 we integrate the particle equations of translational and rotational motion to obtain the location as well as the linear and angular velocities of the particles. We use the drag $\mathbf{F}_{d2}$ and lift $\mathbf{F}_l$ force models that account for particle distance from the bed (equations 12 and 16, also see figure 2a). This numerical setup is well suited for bedload-dominated sediment transport and will be used in the subsequent simulations of cases EL1-EL4. Case EL3a is the same as EL3 except in that the drag force model $\mathbf{F}_{d1}$ does not account for particle distance from the bed (see equation 9), and it does not include a lift force model. In case EL3b, we use the same force model as in case EL3 but do not solve the equation for particle angular velocity (equation 7). As a result, torque models are not needed. Case EL3c is the same as EL3b but without including a model for the tangential collision force $\mathbf{F}_c^t$ (equation 35). Case EL3d is the same as EL3c but with no lift force model $\mathbf{F}_l$ and with the drag force model $\mathbf{F}_{d1}$ from equation 9. Finally, case EL3e (resp. El3f) is the same as EL3 (resp. EL3c) but with no lift force model $\mathbf{F}_l$. The objective of this set of simulations is to test the effect of different components of the force/torque model on bedload-dominated sediment transport by comparing the mean sediment flux and excess Shields stress to those predicted by [4].

Figure 3 shows the streamwise particle flux $\langle q_x \rangle$ as a function of the streamwise excess Shields stress $\langle \theta_x \rangle - \theta_{cr}$ for all simulations. The inset shows a closeup view of the cases shown in Table 4, where different components of the force/torque model are tested. Comparing the different cases in the inset it can be observed that there are small differences and the largest difference is in the streamwise particle flux $\langle q_x \rangle$ of EL3b. Before we investigate the mechanisms responsible for such differences, it is important to establish the vertical and horizontal error bars associated with these data points. The sample size used in the calculation

Case	Particle motion equations.	Particle Models
$EL3$	$\mathbf{x}_p$: 5 ; $\mathbf{v}_p$: 6 ; $\boldsymbol{\omega}_p$: 7	Forces: $\mathbf{F}_{un}$: 8; $\mathbf{F}_{d2}$: 12; $\mathbf{F}_l$: 16; $\mathbf{F}_{am}$: 21; $\mathbf{F}_b$: 22; $\mathbf{F}_c^n$: 30; $\mathbf{F}_c^t$: 35 Torques: $\mathbf{T}_h$: 36; $\mathbf{T}_c$: 40; $\mathbf{T}_r$: 41
$EL3$a	$\mathbf{x}_p$: 5 ; $\mathbf{v}_p$: 6 ; $\boldsymbol{\omega}_p$: 7	Forces: $\mathbf{F}_{un}$: 8; $\mathbf{F}_{d1}$: 9; $\mathbf{F}_l$: $-$; $\mathbf{F}_{am}$: 21; $\mathbf{F}_b$: 22; $\mathbf{F}_c^n$: 30; $\mathbf{F}_c^t$: 35 Torques: $\mathbf{T}_h$: 36; $\mathbf{T}_c$: 40; $\mathbf{T}_r$: 41
$EL3$b	$\mathbf{x}_p$: 5 ; $\mathbf{v}_p$: 6	Forces: $\mathbf{F}_{un}$: 8; $\mathbf{F}_{d2}$: 12; $\mathbf{F}_l$: 16; $\mathbf{F}_{am}$: 21; $\mathbf{F}_b$: 22; $\mathbf{F}_c^n$: 30; $\mathbf{F}_c^t$: 35 Torques: $-$
$EL3$c	$\mathbf{x}_p$: 5 ; $\mathbf{v}_p$: 6	Forces: $\mathbf{F}_{un}$: 8; $\mathbf{F}_{d2}$: 12; $\mathbf{F}_l$: 16; $\mathbf{F}_{am}$: 21; $\mathbf{F}_b$: 22; $\mathbf{F}_c^n$: 30; $\mathbf{F}_c^t$: $-$ Torques: $-$
$EL3$d	$\mathbf{x}_p$: 5 ; $\mathbf{v}_p$: 6	Forces: $\mathbf{F}_{un}$: 8; $\mathbf{F}_{d1}$: 9; $\mathbf{F}_l$: $-$; $\mathbf{F}_{am}$: 21; $\mathbf{F}_b$: 22; $\mathbf{F}_c^n$: 30; $\mathbf{F}_c^t$: $-$ Torques: $-$
$EL3$e	$\mathbf{x}_p$: 5 ; $\mathbf{v}_p$: 6 ; $\boldsymbol{\omega}_p$: 7	Forces: $\mathbf{F}_{un}$: 8; $\mathbf{F}_{d2}$: 12; $\mathbf{F}_l$: $-$; $\mathbf{F}_{am}$: 21; $\mathbf{F}_b$: 22; $\mathbf{F}_c^n$: 30; $\mathbf{F}_c^t$: 35 Torques: $\mathbf{T}_h$: 36; $\mathbf{T}_c$: 40; $\mathbf{T}_r$: 41
$EL3$f	$\mathbf{x}_p$: 5 ; $\mathbf{v}_p$: 6	Forces: $\mathbf{F}_{un}$: 8; $\mathbf{F}_{d2}$: 12; $\mathbf{F}_l$: $-$; $\mathbf{F}_{am}$: 21; $\mathbf{F}_b$: 22; $\mathbf{F}_c^n$: 30; $\mathbf{F}_c^t$: $-$ Torques: $-$

Table 4: Cases performed for sensitivity analysis of the force and torque models. In each case, the equation number of each model is also provided.

of the ensemble averages $\langle q_x \rangle$ and $\langle \theta_x \rangle - \theta_{cr}$ consists of 5.6 million data points. These data points correspond to 330×330 grid points in the horizontal plane and 51 time instances equally spread over 1.5 time units. When the sample size is tripled with the use of 151 time instances instead of 51, the statistics remains nearly unchanged. For example for case EL3, we find $\langle q_x \rangle$ and $\langle \theta_x \rangle$ to differ by less than 0.12% and 0.025%, respectively. Thus, the error bars associated with the data points shown in Figure 3 are quite small.

Comparing cases EL3 and EL3e, we find the lift force to substantially reduce the sediment flux, namely by 40%. A similar effect is also observed by comparing cases EL3c and EL3f, where the lift force model in the latter is also omitted. Here also we find a sediment flux reduction of approximately 43%. Inspecting both cases that do not possess a lift force model, namely EL3a and EL3e, we see that the drag force model equation 9 results in a particle flux increase of approximately 21%. A similar conclusion can be drawn for cases EL3d and EL3f where the drag model, equation 9, in the absence of lift force, particle rotation, and tangential collision, results in a particle flux increase of 15%. The difference between the two drag models on the mean Shields stress is quite small.

On the other hand, a more significant difference can be seen when particle angular velocity is not computed (case EL3b). Comparing cases EL3 and EL3b we find that sediment flux decreases by $\approx 68\%$ in the latter. In EL3b, while particles are not allowed to rotate, the tangential collision force is still computed, thus reducing the sliding motion possibility of a particle as well. This contributes to a substantially lower sediment flux. In contrast, in case EL3c, though particles are not allowed to roll, the tangential collision force is also not taken into account. In this case the sediment flux changes little compared to case EL3 where the rotational motion and tangential force are taken into account. Thus, in case EL3c, the reduction in streamwise sediment flux due to lack of rolling motion is compensated by allowing the particle to freely slide without the penalty of a tangential force. This small difference can also be seen with the use of the quasi-steady force model in cases EL3a and EL3d, where the average streamwise sediment flux is nearly the same.

It can be observed that the average excess Shields stress of case EL3c is noticeably higher than that of case EL3, and correspondingly $\langle \theta_x \rangle - \theta_{cr}$ of case EL3d is higher than EL3a. This increase in Shields stress can be explained in terms of global energy balance. Due to the constancy of applied pressure gradient, the streamwise momentum supplied remains the same in all cases considered. The energy supplied is balanced by the dissipative processes associated with the form drag and the shear stress in the fluid and with the dissipation associated with the normal and tangential collisional processes. Thus, with the elimination of the tangential collisional force, the corresponding dissipation is absent. This contributes to an increase in the excess Shields stress.

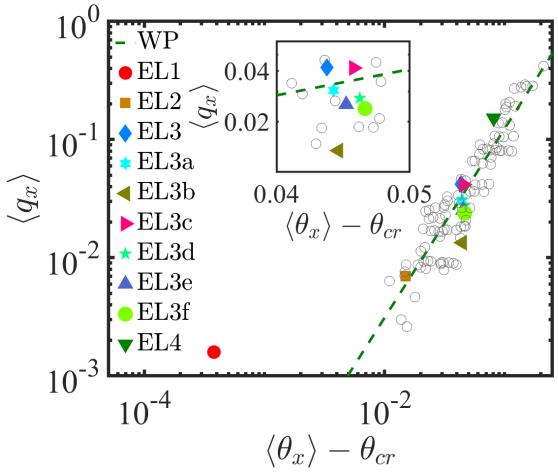

Figure 3: Streamwise particle flux $\langle q_x \rangle$ as a function of excess Shields $\langle \theta_x \rangle - \theta_{cr}$. Inset: enlarged view for the EL3 cases in table 4.

For all cases in Table 4, the probability distribution functions (pdf) for q_x and θ_x are shown in Figure 4. As expected, we find the distribution of q_x from case EL3b to show the largest difference compared to all other cases, while the Shields stress distribution shows little variation among all cases including EL3b. It is interesting to note that $\langle q_x \rangle$ in cases EL3, EL3a, and EL3e is comparable to the corresponding non-rotating cases, namely EL3c, EL3d, and EL3f, respectively. In contrast to the average statistics, it can be observed that the probability of very large sediment flux values slightly increases with the absence of rotation.

The sediment flux represents the collective motion of particles in the entire domain. This includes saltating particles above the sediment bed as well as particles that roll and slide within or at the surface of the bed. In Figure 5, we show the fluid (filled symbols) and particle (open symbols) mean streamwise and positive bed-normal components of velocity at the surface of the particle bed as a function of mean excess Shields stress. When averaged over the horizontal direction, the particle flux $\langle u_p \phi \rangle$ usually attains its maximum value at around the height where $\langle \phi \rangle = 0.1$, hence demonstrating the consistency of the definition of the bed surface. Here $\langle u_{bed} \rangle$ and $\langle w^+_{bed} \rangle$ (resp. $\langle u_{p,bed} \rangle$ and $\langle w^+_{p,bed} \rangle$) denote the mean streamwise and positive bed-normal components of fluid (resp. particle) velocity at the sediment bed surface. Only the positive component of bed-normal velocity is considered since the mean bed-normal velocity of the fluid or the particle phase is identically zero at the bed surface. In fact, in the present simulations and at any instance in time, the bed-normal component of velocity at the bed surface is positive over approximately one half of the domain, and negative over the other half. The corresponding mean values (positive or negative) over the respective grid points are the same.

Since the particles are driven by the flow, the mean fluid velocities are substantially larger than the mean particle velocities. This difference in velocity may however also be caused by the preferential accumulation of particles in low-speed streaks, which are observed in the present simulations. We note that the differences in $\langle \theta_x \rangle - \theta_{cr}$ between the different cases observed in Figure 3 apply to Figure 5a as well. Except for the slightly lower value in case EL3b, the mean streamwise velocity of the fluid at the bed surface is about the same for all other cases. The mean streamwise particle velocity $\langle u_{p,bed} \rangle$ for cases EL3b and EL3d are lower than the results for the corresponding rotation-included cases EL3 and EL3a, which is consistent with the slightly lower mean sediment flux seen in Figure 3. This shows that, the near-bed turbulence remains about the same whether or not particles are allowed rotational degree of freedom, but the effect of this turbulence on particle motion depends on inclusion or exclusion of rotational particle motion. In Figure 5b, the mean excess Shields stress value for postive bed-normal fluid velocity ($\langle \theta_x \rangle - \theta_{cr} \approx 0.038$) is less than the corresponding mean excess Shields stress value averaged over the entire bed surface (see frame a). On the other hand, the mean excess Shields stress in regions of positive wall-normal particle velocity

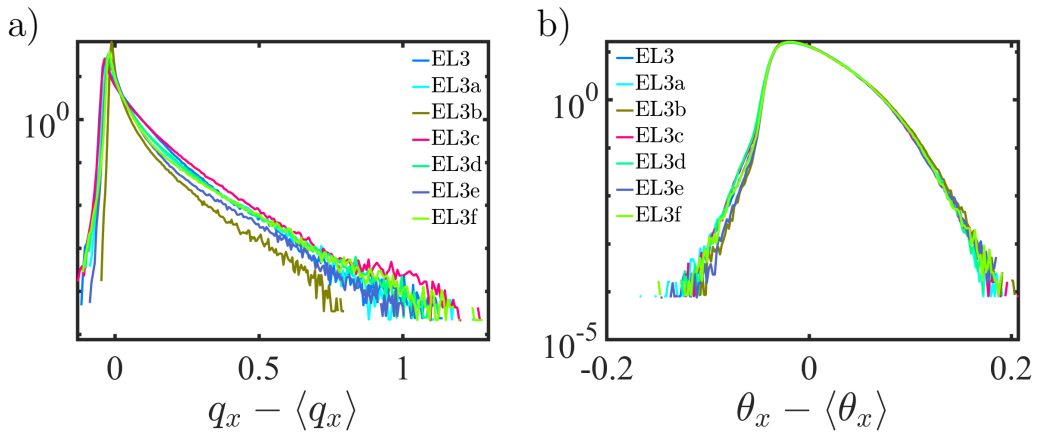

Figure 4: Mean subtracted pdf for a) q_x and b) θ_x.

($\langle \theta_x \rangle - \theta_{cr} \approx 0.055$) is higher. This is to be expected since the grid points over which $w^+_{p,bed}$ is averaged will generally have a larger Shields stress, owing to the fact that particles will only move when the net force exerted on them is above a critical value. Whereas, the grid points over which w^+_{bed} is averaged (i.e., upwelling through the porous bed) will be associated with lower streamwise fluid velocity and thus account for a lower value of $\langle \theta_x \rangle - \theta_{cr}$.

We summarize the results of the sensitivity analysis as follows:

- Since both drag models compare favorably with [4], lying well within the scatter used to generate the WP fit, we conclude that both models are adequate for modeling bedload-dominated sediment transport. We cannot determine if one model is preferable over the other with the data at hand. In fact, it can be conjectured that a variety of reasonably constructed drag and lift models will be adequate, since the differences between them are small.

- Models that do not take particle rotation into account must also omit the tangential collision force from their computations in order to be consistent. Otherwise, if only particle rotation is ignored, then the particle flux will be substantially reduced. This result is due to the loss of the rolling/sliding component of bedload transport. While tangential collisional force hinders sliding motion of particles, lack of rotation hinders rolling motion.

- Models that ignore both particle rotation and tangential collision force appear to correctly predict the mean particle flux, but to overpredict the Shields stress. This overestimation is attributed to the reallocation of dissipative mechanisms associated with particle rotation and tangential collision.

Finally, we note that while the current study focuses on bedload transport in a span of time where the bed remains mostly featureless (almost flat), long time evolution of the simulations indicate that the effect of not including particle rotation could become important at later times, when bedforms appear.

3.2. Effect of coarse graining

The instantaneous sediment flux has been shown to exhibit large scatter when plotted as a function of excess Shields stress [51]. To be specific, the scatter shows that for a particular value of the excess Shields stress, the sediment flux could attain a value over a range of a few orders of magnitude. Additionally, the scatter also shows that the same value of the sediment flux may occur for a range of excess Shields stress of also a few orders of magnitude. This large scatter suggests that temporally and spatially averaged empirical relations such as the WP correlation may not be adequate for use in a local and instantaneous setting. This is because such correlations have a one to one relation between excess Shields stress and sediment flux.

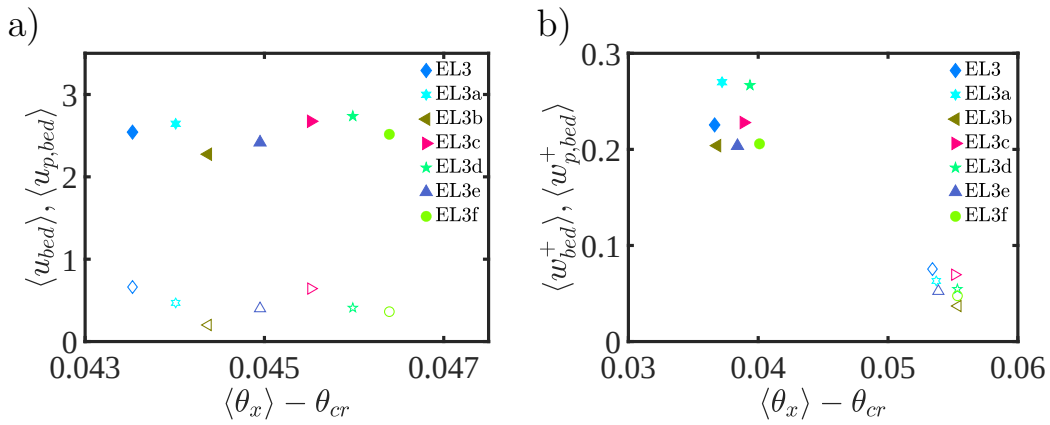

Figure 5: a)Time- and space-averaged streamwise component of fluid, u_{bed} (filled symbols) and particle $u_{p,bed}$ (open symbols) velocities at the bed surface. b) Time- and space-averaged positive bed-normal component of fluid, w^+_{bed} (filled symbols) and particle $w^+_{p,bed}$ (open symbols) velocities at the bed surface.

To reduce the scatter and render WP correlation more applicable, coarse graining may be used. Coarse graining consists of averaging local quantities such as Shields stress or sediment flux over an area so as to include a relatively large number of sediment grains in obtaining the average. By doing so, coarse-grained quantities reflect the collective behavior of particles and reduce variability due to turbulent fluctuations and particle pocket geometry. The larger the area over which the averaging is conducted, the smaller the net effects of turbulent fluctuations and particle pocket geometry.

Figure 6 shows a view of the entire particle bed from case EL3 with two enlarged views with different perspectives, namely panels A ($0 < x < 4$, $1 < y < 2$) and G. Figure 6 also shows vertical slices bisecting the enlarged view A (at $y = 1.5$). The slices correspond to iso-contours of B) streamwise fluid velocity, C) vertical fluid velocity, D) particle volume fraction, E) streamwise particle velocity multiplied by particle volume fraction, and F) vertical particle velocity multiplied by particle volume fraction. We observe from panels B and C that variations in streamwise fluid velocity at the particle bed surface (marked by the white line) occur at a lower spatial frequency compared to variations in vertical fluid velocity at the particle bed surface. We also observe that regions of intense particle transport (identified by the red color in panel E) occur when a region of high momentum in the bulk of the flow penetrates into the bed. This corresponds to the region in panel B where the red iso-surface is in contact with the particle bed surface downstream of the relatively large green patch. We also observe the particles colored in red within this region in panels A and G to indicate saltating sediment transport (see dashed purple circles in both panels which correspond to the same region). Furthermore, at the time instance shown, we find the regions of intense particle transport to occur at various locations over the bed as inferred by the saltating red-colored particles in the full view of the particle bed.

EE simulations where individual particles are not tracked must enforce a Shields-dependent slip velocity at the sediment bed surface [51]. Figure 6 suggests that EE simulations must use coarse-graining so that fluctuations in bed surface fluid velocities and particle flux are minimized. Based on the nature of fluctuations in Figure 6, we find that variations in w_{bed} will quickly diminish compared to variations in u_{bed} as higher levels of coarse graining is implemented. This is due to the fact that variations in w_{bed} occur with a relatively high spatial frequency as previously mentioned.

In Figure 7, we show the scatter plot of the the coarse-grained streamwise component of flux ($\hat{q}_x$) versus coarse-grained streamwise component of excess Shields stress ($\hat{\theta}_x - \theta_{cr}$). Here, coarse-grained quantities are denoted by a hat symbol and are defined as

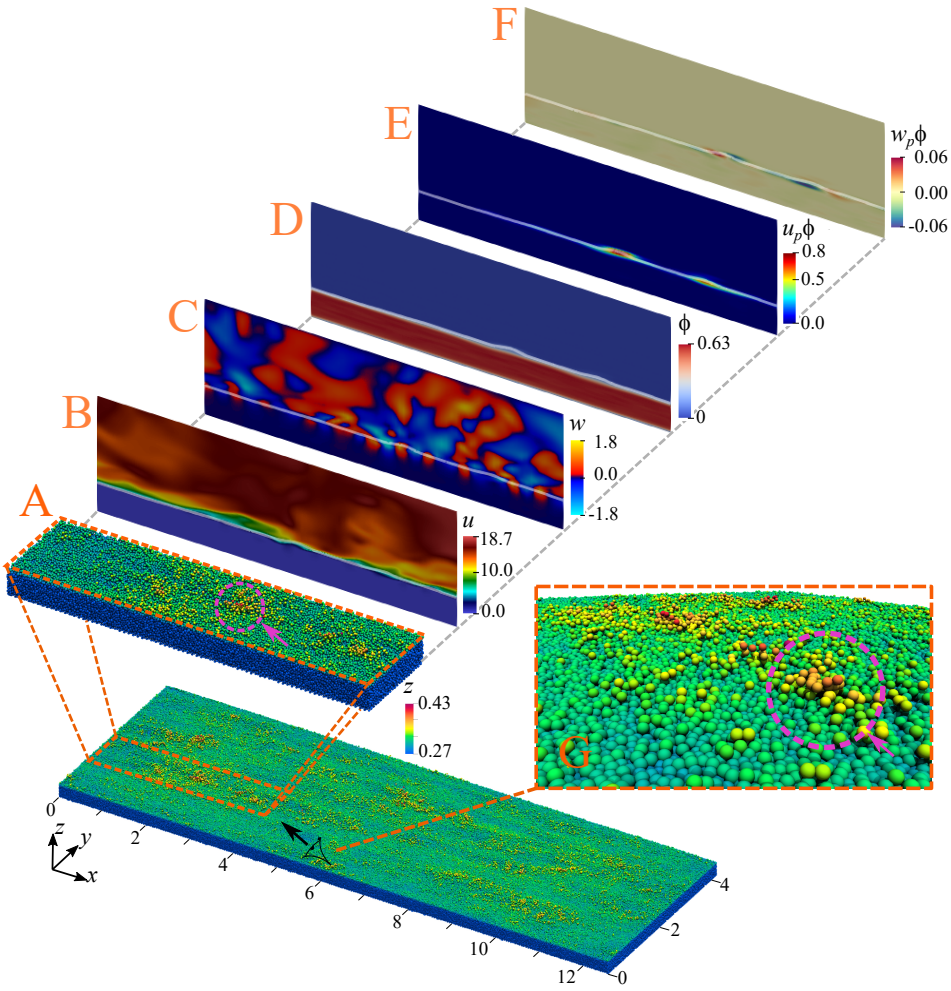

Figure 6: Full view of the particle bed from case EL3 with particles colored by their elevation. A) Enlarged view of a portion of the bed ($0 < x < 4$, $1 < y < 2$) from which fluid and particle properties are extracted in the vertical plane ($y = 1.5$). B) Contours of streamwise component of fluid velocity. C) Contours of vertical component of fluid velocity. D) Contours of particle volume fraction. E) contours of $u_p\phi$. E) contours of $w_p\phi$. G) Close-up view with near-bed perspective showing nearly half the particle bed, including the region shown in A.

$$\hat{\zeta}(x,y,t) \quad = \quad \frac{1}{A}\iint_A \zeta(x,y,t)dxdy, \tag{46}$$

where A corresponds to the horizontal area over which the coarse graining is implemented, and ζ represents the coarse-grained variable. Two different levels of coarse graining are shown in panels b and c. While no coarse graining is implemented in panel a. The level of coarse graining may be quantified by the ratio $\gamma = A/d_p^2$. γ thus quantifies the number of particles contained, one layer in depth, within a cross-sectional area of A. In Figure 7, the value of γ is 0.65, 860, and 5071 for panels a, b, and c, respectively.

The effect of coarse graining is evident from Figure 7, where we show a scatter plot colored by number density for the instantaneous coarse-grained sediment flux $\hat{q}_x$ vs the instantaneous coarse-grained excess Shields stress $\hat{\theta}_x - \theta_{cr}$. The dashed line corresponds to the Wong & Parker sediment flux relation [4], and the solid line represents the power-law regression fit to the scatter. We observe the scatter cloud to shrink in size and the number density within the bins to rise as γ increases. We also find the reduction in scatter

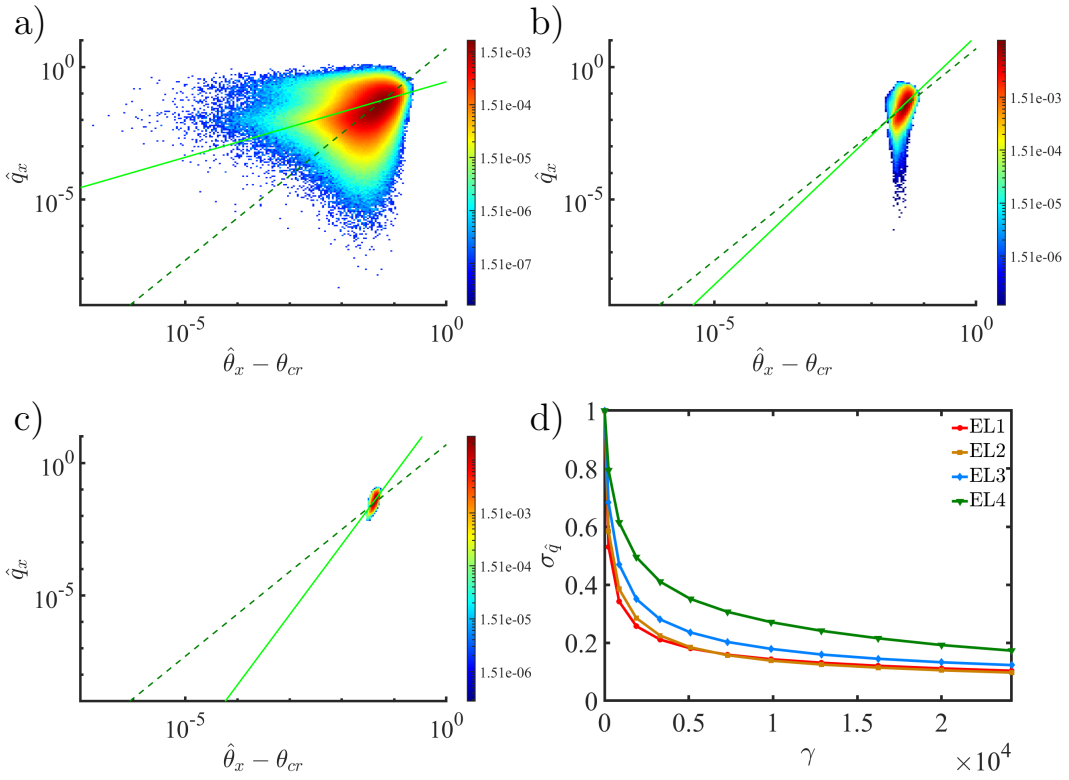

Figure 7: Bin scatter plot colored by number density for flux versus excess Shields stress from EL3 for different levels of coarse graining a) $\gamma = 0.65$, b) $\gamma = 860$, c) $\gamma = 5071$. The larger the value of γ, the smaller the scatter. The dashed and solid lines in panels a, b, and c correspond to WP correlation and the power series regression fit to the scatter, respectively. d) Normalized standard deviation with various levels of coarse graining for $\hat{q}_x$ versus $\hat{\theta}_x - \theta_{cr}$. A total of 62500 bins were used in all scatter plots.

of the Shields stress to be more pronounced than that of the flux, especially at relatively small values of γ. For example, we find the range of scatter in $\hat{\theta}_x - \theta_{cr}$ to be approximately reduced from $[10^{-6}\ 10^{-1}]$, in panel a to $[10^{-2}\ 10^{-1}]$ in panel b. Whereas the reduction in the flux scatter is less pronounced with the range being reduced approximately from $[10^{-7}\ 10^{0}]$, in panel a to $[10^{-5}\ 10^{0}]$ in panel b.

The main purpose of coarse graining is to reduce the variability in the scatter. We use the standard deviation as the metric for quantifying this reduction and assessing the level of coarse graining that would be needed in future studies. A normalized plot of the standard deviation versus γ is shown in Figure 7d. The standard deviation is defined as follows

$$\sigma_{\hat{q}} = \left[\frac{1}{N} \sum_{l=1}^{N} (\hat{q}_x - q_{fit}(\hat{\theta}_x - \theta_{cr})) \right]^{1/2}, \tag{47}$$

where q_{fit} is the value of sediment flux predicted by the power-law fit corresponding to the coarse-grained excess Shields stress. The standard deviation is calculated not with respect to the WP correlation so as not enhance the standard deviation with contribution from differences in the mean.

We observe $\sigma_{\hat{q}}$ to decrease with increasing γ as expected. The rate of decrease is largest for the smallest values of γ and diminishes progressively as γ increases. More specifically, we find a sharp decline in $\sigma_{\hat{q}}$ when γ is of the order of $O(10^3)$ or less, and a mild decline for larger values. We also find $\sigma_{\hat{q}}$ to be also influenced by the ratio Θ/θ_{cr} (see Table 2). The smaller the ratio the larger the reduction in $\sigma_{\hat{q}}$. The non-zero value of $\sigma_{\hat{q}}$ even for large values of γ is indicative of the temporal fluctuation in the value of spatially averaged sediment flux.

Coarse graining can be implemented for all spatially varying quantities. Here we additionally use coarse graining on u_{bed} and w_{bed}, the tangential and bed-normal velocity components of the fluid at the fluid sediment interface, respectively. Both variables are essential for EE sediment transport simulations and are usually set to zero at the fluid sediment interface [52, 53, 54, 55]. While the mean value of w_{bed} is zero at the bed surface, the mean value of u_{bed} is significant compared to the bulk velocity [51]. Both variables also experience large scatter. The normalized standard deviation versus γ is shown in Figure 8. Since the mean value of u_{bed} was found to depend on the excess Shields stress [51], we compute its standard deviation $\sigma_{\hat{u}_{bed}}$ about its power-law fit, similar to the definition given in equation (47). On the other hand, since the average value of w_{bed} over the fluid sediment interface is zero, and therefore independent of the Shields stress, we compute its standard deviation $\sigma_{\hat{w}_{bed}}$ about $w_{bed} = 0$.

For the case of $\sigma_{\hat{u}_{bed}}$, the behavior is similar to that observed in Figure 7d for $\sigma_{\hat{q}}$. Namely, (i) the sharp decline in the standard deviation for small values of γ up to order $O(10^3)$ and the mild decline thereafter, and (ii) Θ/θ_{cr} has a substantial effect on the rate of decline of the standard deviation. For the case of wall normal fluid velocity at the bed, $\sigma_{\hat{w}_{bed}}$ becomes nearly zero upon modest coarse graining indicating that for relatively large coarse-graining areas, the vertical fluid velocity at the bed can be taken to be zero and the bed can be assumed to be non-penetrable. Also, the influence of Θ/θ_{cr} is marginal. The bed normal velocity w_{bed} is influenced by the near-bed Kelvin-Helmholtz (KH) vortices (e.g. [56, 57, 58, 59, 60]). The size of these vortices is on the order of a several particle diameters in length and width [51]. As such, the influence of these rollers on vertical velocity fluctuations will diminish as the coarse graining area A exceeds the size of the rollers. This behavior is evident in $\sigma_{\hat{w}_{bed}}$ in Figure 8b. The relatively fast decay in $\sigma_{\hat{w}_{bed}}$ is also in line with what was observed in Figure 6c where fluctuations from the iso-contours of w_{bed} were shown to occur at a relatively high spatial frequency compared to u_{bed}.

We further note that the spatial variation of w_{bed} from Figure 6c corresponds to the spacing of the KH rollers observed in [51]. More specifically, we find the spacing in Figure 6C to range between 10 and 16 particle diameters, which is similar to the spacing of the KH rollers in [51], which ranged between 12 and 20 particle diameters. This leads us to believe that the reduction in the standard deviation in Figure 8b is due to KH rollers being averaged out.

In Figures 7 and 8, the employed coarse graining area had an aspect ratio of unity, which implies that A corresponds to a square. It should be noted this aspect ratio need not be the case. In fact, we tested additional values of aspect ratio, namely 3 and 1/3 and found that its value is not important, at least in the considered range.

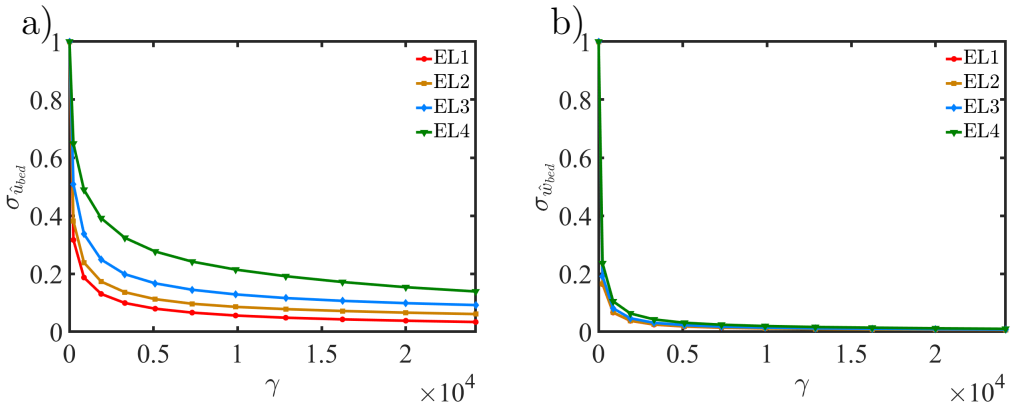

Figure 8: Normalized standard deviation with various levels of coarse graining for a) $\hat{u}_{bed}$ versus $\hat{\theta}_x - \theta_{cr}$, and b) $\hat{w}_{bed}$.

3.3. Effect of time averaging

Another approach for reducing the scatter is through time averaging. Instead of averaging over a window in space at a specific time instance, we average over a window in time at a specific bed location. Time-averaged values are denoted by an overbar and defined as

$$\overline{\zeta}(x,y,t) \quad = \quad \frac{1}{T}\int_T \zeta(x,y,\tau)d\tau. \tag{48}$$

Figure 9 shows the bin scatter plot for flux versus excess Shields stress colored by number density as well as the normalized standard deviation versus the time averaging window, T for the flux and the streamwise and bed-normal components of fluid velocity. The effect of time averaging is similar to what was observed for coarse graining.

Here we should note that the time window for averaging, T, must be chosen such that the particle bed remains macroscopically homogeneous during the averaging period. In the present case, since the bed remains featureless for the entire duration of the simulation, any time span T may be considered. However, once macroscopic features such as bedforms emerge, T cannot be arbitrarily chosen to be too large. In fact, it must remain smaller than the characteristic time scale of bedforms, which may be defined as the ratio of bedform length to celerity. A similar argument may be made for coarse graining where the dimensions of the averaging window along each horizontal direction must remain below the characteristic bedform length along that direction. Though the results of both spatial and temporal averaging are qualitatively similar, quantitative differences can be observed. In particular, temporal averaging is less effective in reducing the fluctuations as measured by the standard deviations. The bed normal velocity fails to converge to zero standard deviation even after long time integration. This is perhaps due to the persistence of long streaky vortical structures and their effect of near-bed fluid and particle velocity.

While the Meyer-Peter and Müller (MPM) equation or the corrected model of Wong & Parker (WPMPM) and other similar correlations were put forth using averaged data to compute the sediment flux, they are presently used to determine local and instantaneous sediment flux in Euler-Euler simulations. This practice is due to the ease of application of these models and for lack of a better alternative [14, 15, 12]. To resolve the flow dynamics in the boundary layer, a fine mesh and a correspondingly small time step are needed in the near-bed region. The fine resolution and small time step may impair the applicability of the aforementioned correlations. This difference can be expected since the correlations are not intended to be used on a local, instantaneous basis. Nevertheless, the degree of departure between the actual sediment flux and that predicted by such models, i.e. the extent of the scatter, has never been quantified and provides a useful measure of how spatially and temporally the sediment flux varies over and above their averaged behavior predicted by the correlations Clearly, coarse graining will reduce the variability of particle flux and other parameters. However, the level of coarse graining that is necessary to improve the applicability of the

aformentioned correlations in the context of Euler-Euler simulations has not been addressed and constitutes one of the objectives of the present study. Following the results in Figure 7, we recommend the coarse graining in Euler-Euler simulations to be on the order of $\gamma = 5000$ (i.e., coarse graining must be on a length scale of the order of hundred particle diameters). Here one could speculate as to why the statistics seem to converge at an order of magnitude increase in the averaging length scale (i.e. the Gaussian filter width). This may be related to the integral length scale of the turbulence or some other turbulent statistic.

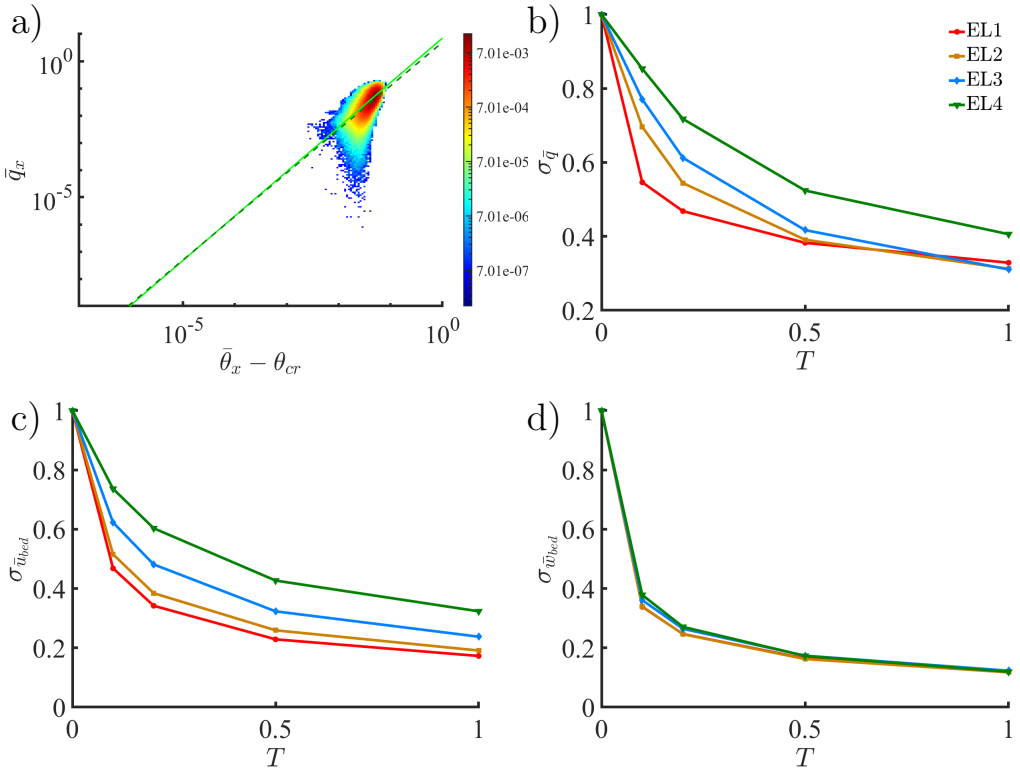

Figure 9: a) Bin scatter plot colored by number density for sediment flux versus excess Shields stress from EL3 for $T = 0.5$. The dashed and solid lines represent the WP correlation and the power series regression fit to the scatter, respectively. The number of bins for the scatter plot is 62500. b), c), and d) Normalized standard deviation for different time averaging intervals T for sediment flux, streamwise component of the bed surface fluid velocity, and normal component of the bed surface fluid velocity, respectively.

4. Conclusions

We presented results from Euler-Lagrange simulations of a turbulent flow over a monodisperse erodible particle bed at a shear Reynolds number of $Re_\tau = 180$ and over a range of Θ/θ_{cr} between 1.32 and 5.98. Two drag models were investigated along with the influence of lift force, particle rotation, and tangential collision force for each model. We find the temporally and spatially-averaged particle flux and excess Shields stress to vary little between the two drag models and to compare well with WP correlation [4]. The simulation results show that ignoring particle rotation, but accounting for tangential collisional force to be inconsistent. Since this prevents both the rolling and sliding particle motion on the bed, the resulting particle flux is substantially lowered. Thus, if the rotational motion of the particle is ignored, it is appropriate to ignore the tangential collisional force as well. This results in a quite accurate mean sediment flux. This indifference is attributed to the fact that particles can now easily slide, when though they are prevented from rolling and as a result the increased sliding transport compensates for the rolling transport. However, the mean excess Shields stress

slightly increases, since without rotational motion and tangential collisional force, inter-particle dissipation decreases, which contributes to a higher fluid shear stress at the bed. Furthermore, we find that ignoring the lift force model, equation 16, which should be applied in conjunction with the drag model of equation 12, results in a substantial reduction of sediment flux.

Empirical relations such as [4, 5] were developed to estimate the mean, time- and space-averaged, sediment flux as a function of the excess Shields stress. However, these relations are used in a local and instantaneous setting where fluctuations due to the turbulent nature of the flow and the stochastic bed arrangement can significantly affect their accuracy. This work explores the possibility of reducing the scatter and departure from empirical correlations in sediment flux as a function of excess Shields stress upon spatial and temporal averaging. The reduction in the scatter was also explored for other quantities of interest such as streamwise and bed-normal fluid velocity at the bed surface. The reduction in scatter was quantified using the standard deviation of the scatter. As far as spatial coarse graining is concerned, we tested averages over rectangular cross-sections of different aspect ratios and observe the results to be insensitive to the shape of the averaging area, but strongly dependent on the size of the averaging area. The reduction in scatter is rapid with an increase in the averaging area when the ratio of averaging area to the square of the particle diameter is relatively small, less than $O(10^3)$. For larger averaging areas, the scatter continues to reduce albeit at a slower rate. The reduction of scatter is more pronounced for smaller ratios of Shields to critical Shields, Θ/θ_{cr}. Similar qualitative conclusions can be drawn for time averaging as well, but in general time-averaging is observed to be less effective than spatial coarse graining in reducing the scatter. Finally, we note that while a large area for coarse graining and a long period for time averaging are preferred to achieve the largest reduction in scatter, the area or the time window over which averaging is performed must ensure that the particle bed is homogeneous within. This is especially important when bedforms emerge. So the dimensions of the area for coarse graining must be less than the characteristic length of bedforms, and the time window for averaging must be less than the characteristic time of bedforms.

Acknowledgments

The authors gratefully acknowledge support from ExxonMobil Upstream Research Company through grant number EM09296. The simulations discussed in this work where performed with the help of the High Performance Computing Center at the University of Florida.

References

[1] J. Salinas, S. Balachandar, M. Shringarpure, J. Fedele, D. Hoyal, M. Cantero, Soft transition between subcritical and supercritical currents through intermittent cascading interfacial instabilities, Proceedings of the National Academy of Sciences 117 (31) (2020) 18278–18284.

[2] W. Wu, S. S. Wang, Y. Jia, Nonuniform sediment transport in alluvial rivers, Journal of hydraulic research 38 (6) (2000) 427–434.

[3] L. C. Van Rijn, et al., Principles of sediment transport in rivers, estuaries and coastal seas, Vol. 1006, Aqua publications Amsterdam, 1993.

[4] M. Wong, G. Parker, Reanalysis and correction of bed-load relation of meyer-peter and müller using their own database, Journal of Hydraulic Engineering 132 (11) (2006) 1159–1168.

[5] E. Meyer-Peter, R. Müller, Formulas for bed-load transport, in: IAHSR 2nd meeting, Stockholm, appendix 2, IAHR, 1948.

[6] S. E. Coleman, B. W. Melville, Initiation of bed forms on a flat sand bed, Journal of Hydraulic Engineering 122 (6) (1996) 301–310.

[7] A. Shields, Application of similarity principles and turbulence research to bed-load movement (1936).

[8] M. Garcia, Sedimentation engineering: processes, measurements, modeling, and practice, American Society of Civil Engineers, 2008.

[9] L. C. v. Rijn, Sediment transport, part ii: suspended load transport, Journal of hydraulic engineering 110 (11) (1984) 1613–1641.

[10] H. Lee, M. Y. Ha, S. Balachandar, Work-based criterion for particle motion and implication for turbulent bed-load transport, Physics of Fluids 24 (11) (2012) 116604.

[11] C. Ancey, Stochastic modeling in sediment dynamics: Exner equation for planar bed incipient bed load transport conditions, Journal of Geophysical Research: Earth Surface 115 (F2) (2010).

[12] N. Zgheib, J. Fedele, D. Hoyal, M. Perillo, S. Balachandar, Direct numerical simulation of transverse ripples: 1. pattern initiation and bedform interactions, Journal of Geophysical Research: Earth Surface 123 (3) (2018) 448–477.
[13] N. Zgheib, J. Fedele, D. Hoyal, M. Perillo, S. Balachandar, Direct numerical simulation of transverse ripples: 2. self-similarity, bedform coarsening, and effect of neighboring structures, Journal of Geophysical Research: Earth Surface 123 (3) (2018) 478–500.
[14] Y.-J. Chou, O. B. Fringer, A model for the simulation of coupled flow-bed form evolution in turbulent flows, Journal of Geophysical Research: Oceans 115 (C10) (2010).
[15] S. Niemann, J. Fredsøe, N. G. Jacobsen, Sand dunes in steady flow at low froude numbers: Dune height evolution and flow resistance, Journal of Hydraulic Engineering 137 (1) (2011) 5–14. doi:https://doi.org/10.1061/(ASCE)HY.1943-7900.0000255.
[16] D. Zwick, S. Balachandar, A scalable euler–lagrange approach for multiphase flow simulation on spectral elements, The International Journal of High Performance Computing Applications 34 (3) (2020) 316–339.
[17] K. Liu, M. Lakhote, S. Balachandar, Self-induced temperature correction for inter-phase heat transfer in euler-lagrange point-particle simulation, Journal of Computational Physics 396 (2019) 596–615.
[18] A. G. Kidanemariam, M. Uhlmann, Interface-resolved direct numerical simulation of the erosion of a sediment bed sheared by laminar channel flow, International Journal of Multiphase Flow 67 (2014) 174–188.
[19] A. G. Kidanemariam, M. Uhlmann, Direct numerical simulation of pattern formation in subaqueous sediment, Journal of Fluid Mechanics 750 (2014).
[20] A. G. Kidanemariam, M. Uhlmann, Formation of sediment patterns in channel flow: minimal unstable systems and their temporal evolution, Journal of Fluid Mechanics 818 (2017) 716–743.
[21] M. Mazzuoli, A. G. Kidanemariam, P. Blondeaux, G. Vittori, M. Uhlmann, On the formation of sediment chains in an oscillatory boundary layer, Journal of Fluid Mechanics 789 (2016) 461–480.
[22] M. Mazzuoli, P. Blondeaux, G. Vittori, M. Uhlmann, J. Simeonov, J. Calantoni, Interface-resolved direct numerical simulations of sediment transport in a turbulent oscillatory boundary layer, arXiv preprint arXiv:1912.00048 (2019).
[23] B. Vowinckel, T. Kempe, J. Fröhlich, V. Nikora, Numerical simulation of sediment transport in open channel flow, in: River flow, CRC Press London, 2012, pp. 507–514.
[24] B. Vowinckel, T. Kempe, J. Fröhlich, V. Nikora, Direct numerical simulation of bed-load transport of finite-size spherical particles in a turbulent channel flow, in: Direct and Large-Eddy Simulation IX, Springer, 2015, pp. 663–669.
[25] N. Zgheib, S. Balachandar, Linear stability analysis of subaqueous bedforms using direct numerical simulations, Theoretical and Computational Fluid Dynamics 33 (2) (2019) 161–180.
[26] G. Kocurek, R. C. Ewing, D. Mohrig, How do bedform patterns arise? new views on the role of bedform interactions within a set of boundary conditions, Earth surface processes and landforms 35 (1) (2010) 51–63.
[27] C. T. Crowe, J. D. Schwarzkopf, M. Sommerfeld, Y. Tsuji, Multiphase flows with droplets and particles, CRC press, 2011.
[28] S. Tenneti, R. Garg, S. Subramaniam, Drag law for monodisperse gas–solid systems using particle-resolved direct numerical simulation of flow past fixed assemblies of spheres, International journal of multiphase flow 37 (9) (2011) 1072–1092.
[29] D. Gidaspow, Multiphase flow and fluidization: continuum and kinetic theory descriptions, Academic press, 1994.
[30] A. Sangani, A. Acrivos, Slow flow through a periodic array of spheres, International Journal of Multiphase Flow 8 (4) (1982) 343–360.
[31] Y. (Yali) Tang, E. (Frank) Peters, J. (Hans) Kuipers, S. (Sebastian) Kriebitzsch, M. (Martin) van der Hoef, A new drag correlation from fully resolved simulations of flow past monodisperse static arrays of spheres, AIChE journal 61 (2) (2015) 688–698.
[32] X. Li, S. Balachandar, H. Lee, B. Bai, Fully resolved simulations of a stationary finite-sized particle in wall turbulence over a rough bed, Physical Review Fluids 4 (9) (2019) 094302.
[33] L. Zeng, S. Balachandar, P. Fischer, F. Najjar, Interactions of a stationary finite-sized particle with wall turbulence, Journal of Fluid Mechanics 594 (2008) 271.
[34] L. Zeng, F. Najjar, S. Balachandar, P. Fischer, Forces on a finite-sized particle located close to a wall in a linear shear flow, Physics of fluids 21 (3) (2009) 033302.
[35] H. Lee, S. Balachandar, Effects of wall roughness on drag and lift forces of a particle at finite reynolds number, International Journal of Multiphase Flow 88 (2017) 116–132.
[36] G. P. Krishnan, D. T. Leighton Jr, Inertial lift on a moving sphere in contact with a plane wall in a shear flow, Physics of Fluids 7 (11) (1995) 2538–2545.
[37] H. Lee, S. Balachandar, Drag and lift forces on a spherical particle moving on a wall in a shear flow at finite re, Journal of Fluid Mechanics 657 (2010) 89.
[38] J. R. Finn, M. Li, S. V. Apte, Particle based modelling and simulation of natural sand dynamics in the wave bottom boundary layer, Journal of Fluid Mechanics 796 (2016) 340–385.
[39] J. Capecelatro, O. Desjardins, An euler–lagrange strategy for simulating particle-laden flows, Journal of Computational Physics 238 (2013) 1–31.
[40] R. A. Bagnold, Experiments on a gravity-free dispersion of large solid spheres in a newtonian fluid under shear, Proceedings of the Royal Society of London. Series A. Mathematical and Physical Sciences 225 (1160) (1954) 49–63.
[41] M. W. Schmeeckle, J. M. Nelson, J. Pitlick, J. P. Bennett, Interparticle collision of natural sediment grains in water, Water Resources Research 37 (9) (2001) 2377–2391.
[42] J. Capecelatro, O. Desjardins, R. O. Fox, Numerical study of collisional particle dynamics in cluster-induced turbulence, Journal of Fluid Mechanics 747 (2014).
[43] S. Balachandar, K. Liu, M. Lakhote, Self-induced velocity correction for improved drag estimation in euler–lagrange point-particle simulations, Journal of Computational Physics 376 (2019) 160–185.

[44] M. I. Cantero, S. Balachandar, G. Parker, Direct numerical simulation of stratification effects in a sediment-laden turbulent channel flow, Journal of Turbulence (10) (2009) N27.
[45] A. T. Patera, A spectral element method for fluid dynamics: laminar flow in a channel expansion, Journal of computational Physics 54 (3) (1984) 468–488.
[46] M. O. Deville, P. F. Fischer, E. H. Mund, High-Order Methods for Incompressible Fluid Flow, Cambridge University Press , , 2002.
[47] D. Zwick, S. Balachandar, Dynamics of rapidly depressurized multiphase shock tubes, Journal of Fluid Mechanics 880 (2019) 441–477.
[48] J. A. Simeonov, S. Bateman, J. Calantoni, Filter width and uncertainty estimation in continuum modeling of particle phases, International Journal of Multiphase Flow (74) (2015) 79–83.
[49] J. Fedele, D. Hoyal, Z. Barnaal, S. Awalt, Experiments on bedforms created by gravity flows, in: EGU General Assembly Conference Abstracts, 2014, p. 4514.
[50] J. J. Fedele, D. Hoyal, Z. Barnaal, J. Tulenko, S. Awalt, et al., Bedforms created by gravity flows, Autogenic dynamics and self-organization in sedimentary systems 106 (2016) 95À121.
[51] L. Guan, J. Salinas, N. Zgheib, S. Balachandar, The role of bed-penetrating kelvin–helmholtz vortices on local and instantaneous bedload sediment transport, Journal of Fluid Mechanics 911 (2021).
[52] N. Zgheib, S. Balachandar, On the role of sidewalls in the transition from straight to sinuous bedforms, Geophysical Research Letters 46 (16) (2019) 9612–9619.
[53] T. Broecker, W. Elsesser, K. Teuber, I. Özgen, G. Nützmann, R. Hinkelmann, High-resolution simulation of free-surface flow and tracer retention over streambeds with ripples, Limnologica 68 (2018) 46–58.
[54] F. Janssen, M. B. Cardenas, A. H. Sawyer, T. Dammrich, J. Krietsch, D. De Beer, A comparative experimental and multiphysics computational fluid dynamics study of coupled surface–subsurface flow in bed forms, Water Resources Research 48 (8) (2012).
[55] A. Yeganeh-Bakhtiary, M. H. Kazeminezhad, A. Etemad-Shahidi, J. H. Baas, L. Cheng, Euler–euler two-phase flow simulation of tunnel erosion beneath marine pipelines, Applied Ocean Research 33 (2) (2011) 137–146.
[56] K. Suga, M. Mori, M. Kaneda, Vortex structure of turbulence over permeable walls, International journal of heat and fluid flow 32 (3) (2011) 586–595.
[57] C. Manes, D. Poggi, L. Ridolfi, Turbulent boundary layers over permeable walls: scaling and near wall structure, Journal of Fluid Mechanics 687 (2011) 141–170.
[58] J. Jimenez, M. Uhlmann, A. Pinelli, G. Kawahara, Turbulent shear flow over active and passive porous surfaces, Journal of Fluid Mechanics 442 (2001) 89.
[59] Y. Kuwata, K. Suga, Lattice boltzmann direct numerical simulation of interface turbulence over porous and rough walls, International Journal of Heat and Fluid Flow 61 (2016) 145–157.
[60] Y. Kuwata, K. Suga, Direct numerical simulation of turbulence over anisotropic porous media, Journal of Fluid Mechanics 831 (2017) 41–71.